HAL open science

High performance flexible hybrid supercapacitors based on nickel hydroxide deposited on copper oxide supported by copper foam for a sunlight-powered rechargeable energy storage system

Min Li, Ahmed Addad, Pascal Roussel, Sabine Szunerits, Rabah Boukherroub

To cite this version:

Min Li, Ahmed Addad, Pascal Roussel, Sabine Szunerits, Rabah Boukherroub. High performance flexible hybrid supercapacitors based on nickel hydroxide deposited on copper oxide supported by copper foam for a sunlight-powered rechargeable energy storage system. Journal of Colloid and Interface Science, 2020, Journal of Colloid and Interface Science, 579, pp.520-530. 10.1016/j.jcis.2020.06.092 . hal-02949089

HAL Id: hal-02949089

https://hal.univ-lille.fr/hal-02949089v1

Submitted on 15 Jul 2022

HAL is a multi-disciplinary open access archive for the deposit and dissemination of scientific research documents, whether they are published or not. The documents may come from teaching and research institutions in France or abroad, or from public or private research centers.

L'archive ouverte pluridisciplinaire **HAL**, est destinée au dépôt et à la diffusion de documents scientifiques de niveau recherche, publiés ou non, émanant des établissements d'enseignement et de recherche français ou étrangers, des laboratoires publics ou privés.

Distributed under a Creative Commons Attribution - NonCommercial 4.0 International License

Version of Record: https://www.sciencedirect.com/science/article/pii/S0021979720308377
Manuscript_40016204735b2cebd464d00973caab65

High Performance Flexible Hybrid Supercapacitors Based on Nickel Hydroxide Deposited on Copper oxide supported by Copper Foam for a Sunlight-Powered Rechargeable Energy Storage System

Min Li,[1] Ahmed Addad,[2] Pascal Roussel,[3] Sabine Szunerits[1] and Rabah Boukherroub[1*]

[1]*Univ. Lille, CNRS, Centrale Lille, Univ. Polytechnique Hauts-de-France, UMR 8520 - IEMN, F-59000 Lille, France*

[2]*Univ. Lille, CNRS, UMR 8207 – UMET, F-59000 Lille, France*

[3]*Univ. Lille, CNRS, ENSCL, Centrale Lille, Univ. Artois, UMR8181, UCCS-Unité de Catalyse et Chimie du Solide, Lille, F-59000, France*

[*]To whom correspondence should be addressed: rabah.boukherroub@univ-lille.fr (R. Boukherroub); Tel: +33 3 62 53 17 24; Fax: 33 3 62 53 17 01.

© 2020 published by Elsevier. This manuscript is made available under the CC BY NC user license
https://creativecommons.org/licenses/by-nc/4.0/

Abstract

Herein, an integrated system combining solar cells with a hybrid supercapacitor device for operating a homemade windmill device was assembled, achieving energy conversion, storage and utilization. As a candidate for positive electrode of hybrid supercapacitor devices, battery-like $Ni(OH)_2$@CuO@Cu binder-free electrode was fabricated by a two-step process at ambient temperature. CuO@Cu was prepared by chemical oxidation method to act as the supporting electrode for electrochemical deposition of $Ni(OH)_2$. Various deposition times (30, 50, 90, 150 and 200s) were investigated to optimize the energy storage characteristics of the resulting $Ni(OH)_2$@CuO@Cu electrode materials. Among all the samples, $Ni(OH)_2$@CuO@Cu-150 exhibited the largest areal capacity of 7063 mC cm^{-2} at 20 mA cm^{-2}, and was therefore chosen as the positive electrode in a hybrid supercapacitor device. Using N-doped reduced graphene oxide on nickel foam (N-rGO/NF) as the negative electrode, a hybrid supercapacitor was assembled. It displayed good flexibility, cycling stability and high areal energy density of 130.4 μWh cm^{-2} at a power density of 1.6 mW cm^{-2}. Two hybrid supercapacitor devices were connected in series to successfully lighten up a red LED for 12min 39s, while three devices assembled in series were able to successfully power a three-digit digital display for 1min 28s. Interestingly, the hybrid supercapacitor device, charged by solar cells, further operated a homemade windmill device for 59s, achieving sunlight-powered integration system. All of the findings suggested the practical application potential of the hybrid supercapacitor based on $Ni(OH)_2$@CuO@Cu composite as energy storage device.

Keywords: *$Ni(OH)_2$; CuO; Copper foam; Flexible Supercapacitors; Sunlight-powered; Energy storage system.*

1. Introduction

In the last few years, the problems associated with environment pollution, fossil fuels decline, and global warming have drawn increasing concern [1, 2]. To pursue a sustainable life, people have concentrated more on clean and low cost energy sources like solar energy, wind energy, rain, tides, waves, geothermal heat and hydrogen energy [3-5]. Furthermore, the development of electric vehicles and new wearable electronics promotes the exploration of flexible energy storage devices with high energy density [6-8]. As energy storage devices, supercapacitors become more and more favored, because of their obvious benefits like low cost, high power density, fast charge-discharge speed, and so on [9, 10]. However, most of supercapacitors encounter the problem of low energy density (*E*) compared with batteries, hindering their widespread application in our daily life [11, 12]. According to the correlation of energy density with capacitance and potential ($E = \frac{1}{2}CV^2$), high energy density can be reached through enhancing the capacitance (C) and/or the operating potential window (V). Hence, constructing a hybrid supercapacitor device represents an attractive route to broaden the operating potential window, further enhancing the energy density [13-15].

Usually, a hybrid supercapacitor device consists of a positive battery-like electrode with high capacity, and a negative carbon-based electrode with a wide working potential window [16, 17]. For example, Wang *et al*. constructed a hybrid supercapacitor device by employing metal silicates as an effective positive electrode and activated carbon as negative electrode material in PVA-KOH gel electrolyte, achieving high energy density of 4.6 mWh cm^{-3} [18]. Dong *et al*. assembled NiSi/GO composite//activated carbon (AC) hybrid supercapacitor device, exhibiting an energy density of 0.37 Wh m^{-2} [19]. Zhang *et al*. fabricated a hybrid supercapacitor using NiO/C/rGO and a hierarchical porous carbon derived from sodium citrate, delivering a high energy density of 35.9 Wh kg^{-1} [20]. Among all the battery-like electrode materials, $Ni(OH)_2$ with large theoretical specific capacitance (2082 F g^{-1}) has drawn plenty of interest. Wang *et al*. prepared nanostructured nickel silicate-nickel hydroxide composite (NiSi-$Ni(OH)_2$) with a relatively high charge storage property of 476.4 F g^{-1} at 2 A g^{-1} [21]. Jiang *et al*. fabricated 3D porous $Ni(OH)_2$/Ni electrode and achieved a specific

capacity of 414 mC cm^{-2} at 10 mA cm^{-2} [22]. Xiong *et al*. reported the formation of ultrathin $Ni(OH)_2$ nanosheets on nickel foam (NF), demonstrating an areal capacity of 2160 mC cm^{-2} at 2 mA cm^{-2} [23]. Zou *et al*. synthesized $Ni(OH)_2$ nanosheets on electrochemically activated carbon cloth, exhibiting a specific capacity of 918 mC cm^{-2} at 2 mA cm^{-2} [24]. Shi *et al*. prepared $Ni(OH)_2$-Cu electrode, which delivered 3464 mC cm^{-2} at 1 mA cm^{-2} [25]. Even though the electrode materials achieved a good performance, the recorded capacity was far below the theoretical value. Therefore, there is enough room for alternative methods to improve the properties of Ni-based electrodes.

In this study, we synthesized $Ni(OH)_2$ through electrochemical deposition on Cu foam current collector, owing to its three-dimensional (3D) structure and good conductivity. Before $Ni(OH)_2$ electrochemical deposition, CuO was formed on Cu foam (CuO@Cu) by chemical oxidation, followed by thermal annealing at 190 ^{o}C for 3 h. The electrodeposition of $Ni(OH)_2$ was investigated for various time spans (30, 50, 90, 150 and 200 s) to gain some insights on the effect of deposition time on the electrochemical properties of the resulting $Ni(OH)_2$@CuO@Cu electrode materials. Among them, $Ni(OH)_2$@CuO@Cu-150 composite exhibited the largest active surface area of 512.6 cm^2 and areal capacity of ~7063 mC cm^{-2} at 20 mA cm^{-2}. However, in absence of CuO nanostructured layer, $Ni(OH)_2$@Cu-150 achieved an areal capacity of 3667.2 mC cm^{-2} at 20 mV s^{-1}, which is much lower than that of $Ni(OH)_2$@CuO@Cu-150 (7742 mC cm^{-2} at 20 mV s^{-1}), indicating the importance of CuO nanostructured layer to facilitate electron and ion transfer to further enhance the electrochemical performance of the electrodes. Hence, $Ni(OH)_2$@CuO@Cu-150 was investigated as a positive electrode to assemble a hybrid supercapacitor device, while N-doped reduced graphene oxide coated on nickel foam (N-rGO/NF) was applied as a negative electrode. The device displayed a large areal energy density of 130.4 μWh cm^{-2} at a power density of 1.6 mW cm^{-2}. For practical applications, two hybrid supercapacitor devices were assembled in series to successfully lighten up a red LED for 12 min 39 s. In addition, a three-digit digital display was powered for 1 min 28 s using three devices in series. Finally, a sunlight-powered integration system based on the hybrid supercapacitor device, solar cells, and a homemade windmill device was constructed. The hybrid supercapacitor was charged by the solar cell, which further powered the windmill device and ensured its continuous

operation for 59 s, indicating the successful practical application of the hybrid supercapacitors based on $Ni(OH)_2$@CuO@Cu composites as energy storage devices.

2. Experimental section

2.1 Materials and methods

All the reagents were of analytical grade and used without any further purification. Nickel(II) nitrate tetrahydrate [$Ni(NO_3)_2 \cdot 4H_2O$], sodium hydroxide (NaOH), ammonium persulphate [$(NH_4)_2S_2O_8$], hydrochloric acid (HCl) and acetone were obtained from Sigma-Aldrich (France).

Copper foam (Cu foam) was purchased from Kunshan Guangjiayuan new materials Company (China). Graphene oxide (GO) was purchased from Graphitene (UK). Nickel foam (NF) was obtained from Jiayisheng Company (China).

The water used throughout the experiments was purified with a Milli-Q system from Millipore Co. (resistivity = 18 MΩ.cm)

2.2 Synthesis of N-doped reduced graphene oxide (N-rGO)

N-rGO was prepared by hydrothermal reduction of graphene oxide (GO) in presence of hydrazine monohydrate ($NH_2NH_2 \cdot H_2O$). Typically, 100 mg of GO were dissolved in 50 mL of Milli-Q water and sonicated for 2 h to form a homogeneous GO suspension (2 mg mL^{-1}), followed by the addition of 0.5 M hydrazine monohydrate. The resulting mixture was poured into a 100 mL Teflon-lined autoclave and heated at 160 ºC for 3 h. After cooling to room temperature, N-rGO was aged in Milli-Q water for 72 h and the water was changed every 24 h. Finally, the product was collected by the freezing-dry method for 72 h.

2.3 Synthesis of $Ni(OH)_2$@Cu-150

$Ni(OH)_2$@Cu-150 was synthesized through electrochemical deposition by applying Cu foam, platinum foil and Ag/AgCl respectively as the working, counter, and reference electrodes. The electrolyte was $Ni(NO_3)_2 \cdot 6H_2O$ (0.3 M, 40 mL). The potentiostatic deposition was carried out at -1 V *vs.* Ag/AgCl for 150 s. The resulting $Ni(OH)_2$@Cu-150 sample was rinsed with MQ water, and dried in ambient air.

2.4 Synthesis of CuO@Cu

CuO@Cu was prepared by chemical oxidation of Cu foam at room temperature (RT), followed by thermal annealing at 190 °C for 3 h. Cu foam (1×3 cm^2) was washed sequentially before use with HCl (2 M), acetone and MQ water under sonication for 10 min each. Then, an aqueous solution (40 mL) of 8 mM $(NH_4)_2S_2O_8$ and 60 mM NaOH was prepared to serve as the alkaline oxidative etchant solution. The clean Cu foam was placed in the above solution for 20 min to produce $Cu(OH)_2$@Cu with a blue color. Furthermore, the $Cu(OH)_2$@Cu sample was annealed at 190 ºC for 3 h to produce CuO@Cu.

2.5 Synthesis of $Ni(OH)_2$@CuO@Cu

$Ni(OH)_2$@CuO@Cu composite materials were synthesized through electrochemical deposition by applying CuO@Cu foam, platinum foil and Ag/AgCl respectively as the working, counter, and reference electrodes. The electrolyte was $Ni(NO_3)_2 \cdot 6H_2O$ (0.3 M, 40 mL). The potentiostatic deposition was carried out at -1 V *vs.* Ag/AgCl for 30, 50, 90, 150 and 200 s to afford respectively $Ni(OH)_2$@CuO@Cu-30, $Ni(OH)_2$@CuO@Cu-50, $Ni(OH)_2$@CuO@Cu-90, $Ni(OH)_2$@CuO@Cu-150 and $Ni(OH)_2$@CuO@Cu-200. The resulting $Ni(OH)_2$@CuO@Cu samples were rinsed with MQ water, and dried in ambient air.

2.6 Assembly of a hybrid supercapacitor device

A hybrid supercapacitor was assembled using $Ni(OH)_2$@CuO@Cu-150 (positive electrode), N-rGO (negative electrode), and a filter paper (separator) immersed into 2 M KOH aqueous solution overnight. The current collector (nickel foam) was coated with N-rGO and polyvinylidene difluoride (PVDF) in a mass ratio of 8:2.

2.7 Construction of a sunlight-powered energy storage system

A sunlight-powered energy storage system was constructed by combining the as-prepared hybrid supercapacitor device with two solar cells (SC-3012-2A) obtained from abandoned solar-powered toys. Furthermore, a home-designed windmill device including an engine (1.5-9 V) and a windmill was prepared, which was powered by the hybrid supercapacitor device.

3. Results and discussion

The main target of the present work was to prepare a highly performant positive electrode for hybrid supercapacitors and further use it for the construction of a sunlight-powered rechargeable energy storage system. Ni-based electrodes display high theoretical capacitance values. Therefore, we investigated $Ni(OH)_2$ modified CuO@Cu [$Ni(OH)_2$@CuO@Cu] as a binder-free electrode for supercapacitors. As illustrated in **Figure 1**, Cu foam was partially oxidized at ambient temperature to produce $Cu(OH)_2$@Cu sample with a blue-grey color (**Figure S1b**). The chemical oxidation reaction could be described using equation (1). The $Cu(OH)_2$@Cu sample was further annealed at 190 ºC for 3 h to form CuO@Cu (equation 2) (**Figure S1c**) with improved electrochemical characteristics (**Figure S2**). $Ni(OH)_2$ was deposited on CuO@Cu at -1 V *vs.* Ag/AgCl for 30, 50, 90, 150 and 200 s to form $Ni(OH)_2$@CuO@Cu-30, $Ni(OH)_2$@CuO@Cu-50, $Ni(OH)_2$@CuO@Cu-90, $Ni(OH)_2$@CuO@Cu-150 and $Ni(OH)_2$@CuO@Cu-200, respectively. $Ni(NO_3)_2 \cdot 6H_2O$ (0.3 M, 40 mL) was the electrolyte, which provided Ni^{2+} and OH^- (equation 3) during the whole deposition process.

$$Cu + (NH_4)_2S_2O_8 + 4NaOH \rightarrow Cu(OH)_2 + 2Na_2SO_4 + 2NH_3 + 2H_2O \quad (1)$$

$$Cu(OH)_2 \xrightarrow{190\ ^oC} CuO + H_2O \quad (2)$$

$$NO_3^- + H_2O + 2e^- = NO_2^- + 2OH^- \quad (3)$$

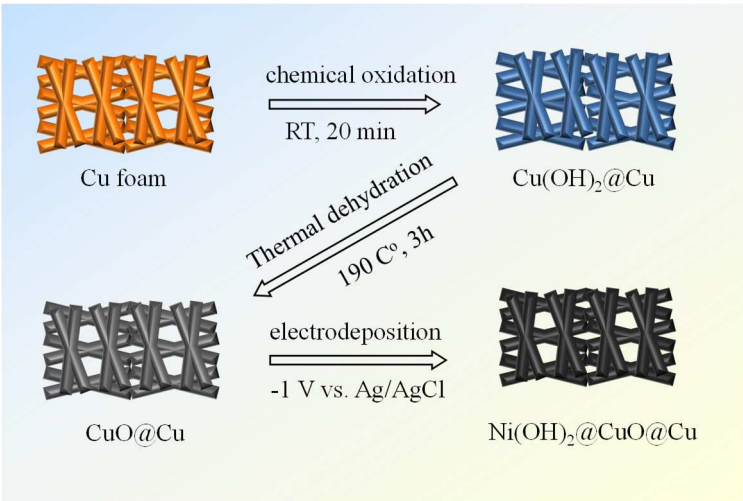

Figure 1: Illustration of the synthesis of $Ni(OH)_2$@CuO@Cu electrode.

To investigate the crystallinity of the samples, X-ray diffraction (XRD) patterns were acquired. All the results are displayed in **Figure S3**, from which we can see peaks due to CuO at 35.5°, 38.7°, 38.9°, 48.7°, 61.5° and 67.9° assigned to the (-111), (111), (200), (-202), (-113), (-311) and (113) planes, respectively (JCPDS No. 41-0254). However, there are no obvious peaks of $Ni(OH)_2$, suggesting poor crystallinity of the material.

Scanning electron microscopy (SEM) was further recorded to gain insight on the morphology of the composites. **Figure 2a**,**b** displays the SEM images of CuO@Cu where 1-dimensinal (1D) CuO nanowires decorated with nanoflowers were observed. This structure was expected to be beneficial to electron and ion transfer. The EDS elemental mapping images of CuO@Cu (**Figure S4**) revealed the homogeneous distribution of Cu and O elements. The SEM images of $Ni(OH)_2$@CuO@Cu-30 and $Ni(OH)_2$@CuO@Cu-50 are exhibited in **Figure 2c** and **Figure S5a**, respectively, showing no obvious difference with the morphology of the CuO@Cu support. This is most likely due to the short deposition time of $Ni(OH)_2$, even though EDS elemental mapping images shown in **Figure S6a**,**b** provided a proof of the existence of Ni element in these composites.

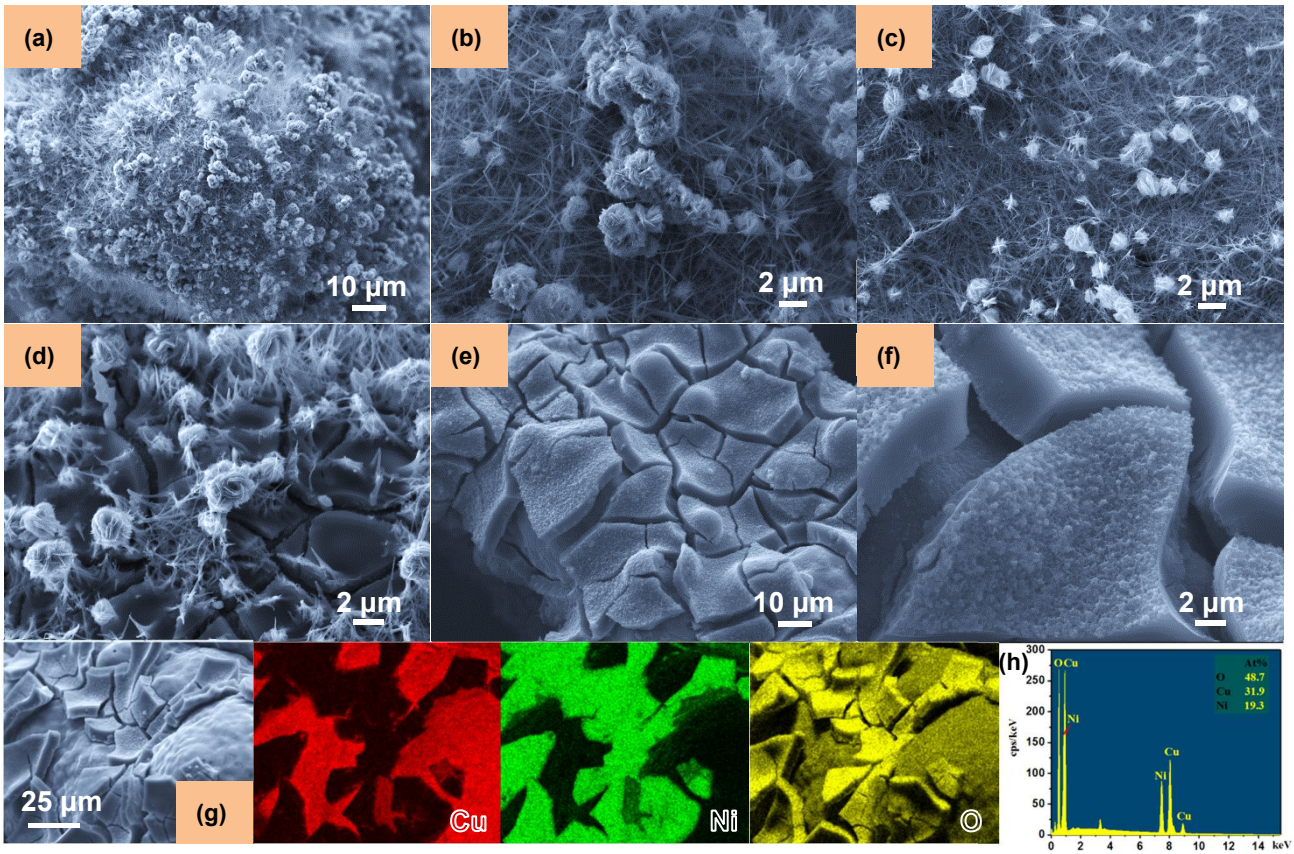

Figure 2: SEM images of (a,b) CuO@Cu foam, (c) $Ni(OH)_2$@CuO@Cu-30, (d) $Ni(OH)_2$@CuO@Cu-90 and (e,f) $Ni(OH)_2$@CuO@Cu-150. (g) EDS elemental mapping images and EDS spectrum of $Ni(OH)_2$@CuO@Cu-150.

At the same time, the EDS spectra in **Figure S7** and elemental composition (**Table S1**) also demonstrated the difference between CuO@Cu, $Ni(OH)_2$@CuO@Cu-30 and $Ni(OH)_2$@CuO@Cu-50, revealing 1.2 and 4.3 at.% of Ni element in $Ni(OH)_2$@CuO@Cu-30 and $Ni(OH)_2$@CuO@Cu-50, respectively, confirming $Ni(OH)_2$ successful deposition on CuO@Cu. With increasing the deposition time to 90 s, apparent changes appeared on the sample morphology. $Ni(OH)_2$ exists obviously and covers the CuO nanowires partly, with the nanoflowers on the surface much like the muddy flowers (**Figure 2d**). The elemental mapping results showed the presence of Ni, Cu and O elements (**Figure S6**). There was an increase of Ni element content, which accounted for 13.7 at.%. Moreover, **Figure 2e**,**f** and **Figure S8** illustrate the SEM images of $Ni(OH)_2$@CuO@Cu-150, in which a thick $Ni(OH)_2$ film consisting of numerous nanopores covers all the CuO nanostructured layer, forming a "dry land"-type architecture, paved on the Cu foam surface. The thick $Ni(OH)_2$@CuO film presents cracks and is partially scratched, which can offer channels for electrolyte diffusion during electrochemical measurements. Notably, some thick $Ni(OH)_2$@CuO pieces fall off on the surface of Cu foam. EDS elemental mapping images and EDS spectrum in **Figure 2g**,**h** revealed that the Ni, Cu and O elements are homogeneously distributed on the material and the Ni content increased to 19.3 at.%. However, the atomic concentration of Ni element in $Ni(OH)_2$@CuO@Cu-200 (20.2 at.%) did not increase much, as compared to $Ni(OH)_2$@CuO@Cu-150; this was most likely due to falling off of the thick $Ni(OH)_2$@CuO piece on Cu foam, as seen in the SEM image in **Figure S5b** and EDS elemental mapping images in **Figure S6d**.

Fourier transform infrared (FTIR) analysis of $Ni(OH)_2$@CuO@Cu-150 was conducted in the 650-4000 cm^{-1} frequency range. The FTIR spectrum in **Figure S9** comprises a few stretching vibration bands. The peak at ~3410 cm^{-1} is the O-H stretching vibration, arising from interlayer water molecules and metal-hydroxyl groups, and the band centered at ~1619 cm^{-1} is assigned to the bending vibration of water [26]. The band located at 1322 cm^{-1} is

attributed to the vibration of interlayer NO_3^- anions from the nickel salt precursor [27].

Furthermore, X-ray photoelectron spectroscopy (XPS) analysis was acquired to evaluate the chemical composition of the samples [28, 29]. From the survey spectra of CuO@Cu (**Figure S10**) and $Ni(OH)_2$@CuO@Cu-150 (**Figure 3**), we can see obviously that there are Cu_{2p} and O_{1s} elements for both samples, along with Ni_{2p} element in $Ni(OH)_2$@CuO@Cu-150 composite, consistent with the EDS elemental mapping results in **Figures S4**, **S6** and **2g**.

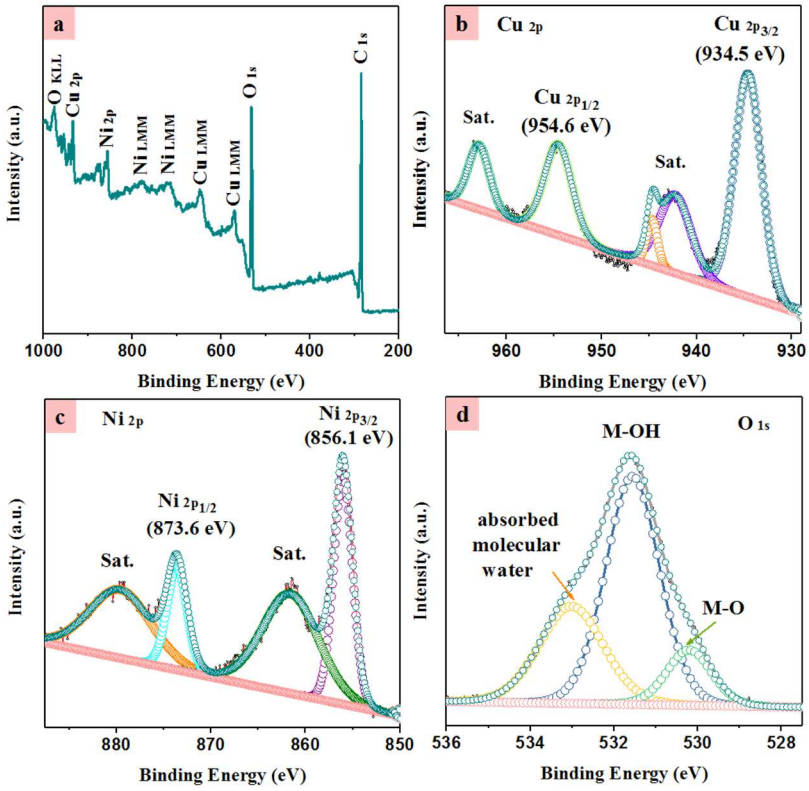

Figure 3: XPS analysis of $Ni(OH)_2$@CuO@Cu-150: (a) Survey spectrum, and core-level spectra of (b) Cu_{2p}, (c) Ni_{2p} and (d) O_{1s}.

The high resolution spectrum of the Cu_{2p} in $Ni(OH)_2$@CuO@Cu-150 (**Figure 3b**) comprises $Cu_{2p3/2}$ and $Cu_{2p1/2}$ peaks respectively at 934.5 and 954.6 eV, and two satellite peaks at ~942.4, and 963.0 eV. Similarly, from **Figure S10b**, we can see that the Cu_{2p} high-resolution spectrum of CuO@Cu can be deconvoluted in two peaks ascribed to $Cu_{2p3/2}$ and $Cu_{2p1/2}$ at respectively 933.7 and 953.7 eV along with two satellite peaks at 943.5 and 962.1 eV, indicating the existence of CuO [30]. There is a small apparent shift in the binding energy compared with $Ni(OH)_2$@CuO@Cu-150, which can be assigned to the interaction between $Ni(OH)_2$ and CuO. **Figure 3c** depicts the core-level spectrum of Ni_{2p}. It consists of

two typical peaks corresponding to $Ni_{2p3/2}$ and $Ni_{2p1/2}$ at respectively 856.1 and 873.6 eV, and two satellite peaks at 861.6 and 879.8 eV, suggesting the existence of Ni^{2+} oxidation state [5]. Furthermore, the core-level spectrum of the O_{1s} of $Ni(OH)_2$@CuO@Cu-150 (**Figure 3d**) can be curve-fitted with three components at 530.2, 531.6 and 533.1 eV, ascribed to M-O binding, M-OH binding and physi- and/or chemisorbed molecular water [22, 31], further proving the successful synthesis of $Ni(OH)_2$@CuO@Cu-150 composite. In contrast, the core-level spectrum of the O_{1s} of CuO@Cu (**Figure S10c**) displays a pair of peaks at ~529.6 and 531.1 eV corresponding to Cu=O and intrinsic oxygen defects in the crystal lattice, respectively [32].

All samples obtained in this work were investigated by electrochemical measurements in aqueous KOH (2 M) electrolyte in a classical 3-electrode cell (**Figure 4** and **Figure S11**). **Figure 4a** and **Figure S11** depict the CV curves of all the samples in the potential range of -0.2 to +0.9 V recorded at 20 mV s^{-1}. The presence of redox active peaks for $Ni(OH)_2$@CuO@Cu foam composites is consistent with the following redox process (Eq.4):

$$\mathrm{Ni(OH)_2 + OH^- \leftrightharpoons NiOOH + H_2O + e^-} \quad (4)$$

By varying the deposition time, $Ni(OH)_2$@CuO@Cu composites exhibited different electrochemical performances. Among all samples, $Ni(OH)_2$@CuO@Cu-150 attained the largest current density at 20 mV s^{-1}. The areal capacity values were determined by integrating the area under the CV curves using the following equation: $C = \frac{1}{2Av}\int_{V_L}^{V_U} I(V)dV$, where C (mC cm^{-2}) is the areal capacity, A (cm^{-2}) is the area of active material, v is the scan rate (V s^{-1}), V_U and V_L are the upper and lower voltage limits (V), and I is the current (mA). The results are summarized in **Table S2**, which revealed that $Ni(OH)_2$@CuO@Cu-150 possessed the largest areal capacity of 7742 mC cm^{-2} at 20 mV s^{-1}. Notably, in absence of CuO nanostructured layer on Cu foam, $Ni(OH)_2$@Cu-150 displayed a smaller areal capacity of 3667.2 mC cm^{-2} at 20 mV s^{-1} (**Figure S11**), indicating the importance of CuO layer to facilitate electron and ion transfer to further enhance the electrochemical performance of the electrodes. **Figure 4b** depicts the CV plots of $Ni(OH)_2$@CuO@Cu-150 measured at various scan rates; as the scan rate increases the redox peak potential shifts positively, suggesting

good conductivity of the electrode and facile ion transport kinetics.

GCD plots of all the samples were recorded to assess their performance. As seen in **Figure 4c**, the $Ni(OH)_2$@CuO@Cu-150 composite exhibited the longest discharge time, signifying the largest areal capacity compared with other samples, in accordance with the results of CV curves in **Figure 4a**. Furthermore, the GCD profiles of the electrodes at various current densities were acquired and the corresponding coulombic efficiencies are depicted in **Table S3**. All $Ni(OH)_2$@CuO@Cu composites revealed higher coulombic efficiencies than CuO@Cu.

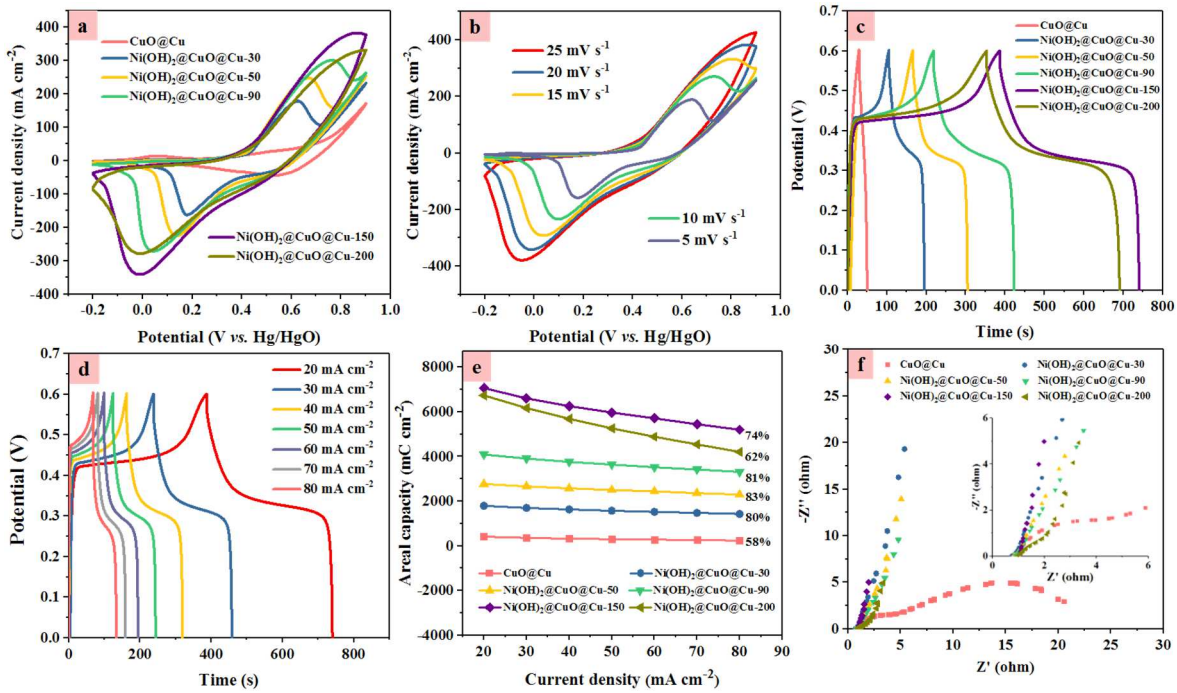

Figure 4: The electrochemical behavior of the different electrodes measured in 2 M KOH aqueous solution. (a) CV plots acquired at 20 mV s^{-1}. (b) CV curves of $Ni(OH)_2$@CuO@Cu-150 recorded at different scan rates. (c) GCD plots of the different electrodes acquired at 20 mA cm^{-2}. (d) GCD profiles of $Ni(OH)_2$@CuO@Cu-150 measured at various current densities. (e) Areal capacity of the electrodes at various current densities. (f) Electrochemical impedance spectra in the 0.01 Hz to 100 kHz frequency range recorded at open circuit potential.

Figure 4d displays the GCD profiles of $Ni(OH)_2$@CuO@Cu-150 composite and the areal capacity values were determined using equation (S2). The composite attained areal capacities

of ~7063, 6606, 6259, 5970, 5709, 5443 and 5203 mC cm^{-2} at 20, 30, 40, 50, 50, 60, 70 and 80 mA cm^{-2}, respectively (see **Figure 4e** and **Table 1**), which are larger than those of some other related works (**Table S4**) [33-37]. One sees that the areal capacity is deposition time dependent. At the initial stage, the areal capacity increases with increasing the deposition time, but saturates when the deposition times exceeds 200 s. This is might be attributed to partial removal of the active materials on Cu foam (**Figure S4b**). Moreover, compared with CuO@Cu, all $Ni(OH)_2$@CuO@Cu composites exhibited improved rate performance (**Figure 4e**).

Table 1. The areal capacity (mC cm^{-2}) of as-obtained composites at various current densities.

Current density (mA cm^{-2}) / **Composites**	20	30	40	50	60	70	80
CuO@Cu	412.8	360	321.6	300	280.8	260.4	240
$Ni(OH)_2$@CuO@Cu-30	1792	1699	1632	1572	1519	1478	1430
$Ni(OH)_2$@CuO@Cu-50	2770	2664	2578	2502	2441	2360	2298
$Ni(OH)_2$@CuO@Cu-90	4092	3906	3758	3642	3521	2360	2298
$Ni(OH)_2$@CuO@Cu-150	7063	6606	6259	5970	5710	5443	5203
$Ni(OH)_2$@CuO@Cu-200	6737	6174	5688	5262	4889	4544	4205

Electrochemical impedance spectroscopy (EIS) analysis in the frequency range (100 kHz to 0.01 Hz) was recorded to gain further insight into the electrochemical processes at different time constants (**Figure 4f**). For all the $Ni(OH)_2$@CuO@Cu composites, the Nyquist plots revealed a very small depressed semicircle (high-to-medium frequency region) related to the electrochemical reaction process, and a straight line (low-frequency region) arising from ion diffusion in the electrode material. **Figure S12b** illustrates the corresponding equivalent circuit, where R_s is the internal resistance, R_{ct} represents the charge-transfer resistance related to the depressed semicircle in the curves, Q is the pseudocapacitance, W_o is the ion transport resistance. Among all $Ni(OH)_2$@CuO@Cu composites, $Ni(OH)_2$@CuO@Cu-150 displayed

the smallest R_{ct} (0.34 ohm cm^{-2}) (**Table S5**) and the biggest slope for the straight line, suggesting favorable access for the charge transfer and ion diffusion. However, for CuO@Cu, there is no ion diffusion process in the 100 kHz to 0.01 Hz frequency range. Two charge transfer processes were observed instead, which take place at the CuO/electrolyte and Cu foam/CuO interfaces. Using the equivalent circuit in **Figure S12a**, R_s = 0.94 ohm cm^{-2}, R_{ct1} = 3.22 ohm cm^{-2} and R_{ct2} = 22.05 ohm cm^{-2} were determined. These values are larger than those recorded for $Ni(OH)_2$@CuO@Cu composites (**Table S5**).

Furthermore, to explore the stability of $Ni(OH)_2$@CuO@Cu-150 composite, 10,000 GCD cycles were recorded at a current density of 80 mA cm^{-2}. As is illustrated in **Figure S13**, the electrode retained about 78% and 61% of the original areal capacity respectively after 2,000 and 10,000 cycles. From SEM images in **Figure S14a,b**, we can see that there is no obvious change of the morphology of $Ni(OH)_2$@CuO@Cu-150 after cycling stability test. The EDS elemental mapping images (**Figure S14c**) demonstrate the uniform distribution of Cu, Ni and O elements, consistent with the XPS results (**Figure S15**) of $Ni(OH)_2$@CuO@Cu-150 after cycling, indicating a good stability.

Furthermore, to investigate the kinetics during the electrochemical reaction, the relationship between log(i) and log(v) for cathodic and anodic peak currents according to the CV curves of $Ni(OH)_2$@CuO@Cu-90 (**Figure S16a**) and $Ni(OH)_2$@CuO@Cu-150 (**Figure 4b**) was studied to determine the capacitive contribution: $i = av^b$, where i stands for the current, v represents the scan rate. When the variable b=1, the electrochemical reaction is controlled by a capacitive process, while when the variable b=0.5, the electrochemical reaction is derived from a semi-infinite diffusion process (Faradaic mode). As displayed in **Figure S16a**, the b-values of $Ni(OH)_2$@CuO@Cu-90 were calculated as 0.56 and 0.60 from the anode and cathode peak currents, respectively, and for $Ni(OH)_2$@CuO@Cu-150 (**Figure 5a**), the b-values were found to be as 0.51 and 0.55 at different scan rates, signifying the contribution of both capacitive and Faradaic battery behaviors in the charge storage process. The whole electrochemical process can be represented by the equation $i = k_1v + k_2v^{1/2}$, and from the relationship of $v^{1/2}$ *vs* $1/v^{1/2}$, we can determine the slope (k_1) and the y-axis intercept (k_2), respectively.

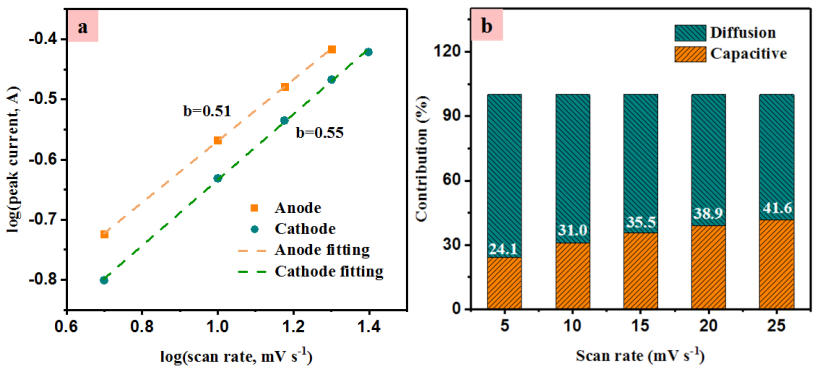

Figure 5: (a) Relationship between log(i) and log(v) of $Ni(OH)_2$@CuO@Cu-150. (b) Capacitive contribution ratio of $Ni(OH)_2$@CuO@Cu-150 at various scan rates.

From **Figure 5b**, we can see that the capacitive contribution ratio for $Ni(OH)_2$@CuO@Cu-150 sample at 5 mV s^{-1} is about 24.1%, and further improves with the increasing the scan rate to attain 41.6% at 25 mV s^{-1}. For the $Ni(OH)_2$@CuO@Cu-90 composite (**Figure S16b**), the capacitive contribution ratio at 2 mV s^{-1} is ~14.5%, and reaches 45.8% at 30 mV s^{-1}. All the results revealed the complex charge storage process based on the combination of capacitive process and diffusion controlled faradaic characteristic with the latter contributing more on the performance.

The real electrochemical effective surface area (A) of the electrodes was investigated by chronocoulometry experiments using 0.1 mM $K_3[Fe(CN)_6]$ in 0.1 M KCl as a probe molecule, and the charge produced by the redox reaction at the electrodes based on the Anson equation (5):

$$Q(t) = \frac{2nFAcD_0^{\frac{1}{2}}t^{\frac{1}{2}}}{\pi^{\frac{1}{2}}} + Q_{dl} + Q_{ads} \quad (5)$$

Where n is the number of electrons transferred, F is the Faraday constant (9.6485×10^5 C mol^{-1}), A is the surface area of the working electrode (cm^2), c is the initial concentration of the redox probe (0.1 mM), D is the diffusion coefficient of the redox probe (7.6×10^{-6} cm^2 s^{-1}), Q_{dl} is the double layer charge, Q_{ads} is the Faradaic charge, charge.

By plotting the Q *vs* $t^{1/2}$, the electrode surface area can be determined from the slope (**Figure S17**). Using equation 5, $Ni(OH)_2$@CuO@Cu-150 displays the largest active surface area of 612.2 cm^2, whereas CuO@Cu, $Ni(OH)_2$@CuO@Cu-30, $Ni(OH)_2$@CuO@Cu-50,

$Ni(OH)_2$@CuO@Cu-90 and $Ni(OH)_2$@CuO@Cu-200 exhibit surface areas of 180, 298.2, 540.1, 586, 123.3 cm^2 respectively, suggesting the favorable electrochemical properties of the $Ni(OH)_2$@CuO@Cu-150 electrode for energy storage.

Consequently, $Ni(OH)_2$@CuO@Cu-150 composite was chosen as the positive electrode to construct a hybrid supercapacitor, according to the schematic diagram presented in **Figure 6a**, while N-rGO coated on NF (N-rGO/NF) acts as the negative electrode. The electrochemical performance was explored in a 2-electrode system. To choose the suitable operating potential window of the hybrid supercapacitor device, as illustrated in **Figure 6b**, the CV plots were acquired at 100 mV s^{-1} in different potential windows. The results indicated that the operating potential window can be extended up to 1.8 V, owing to the large working potential window of N-rGO (**Figure S18**), although there was an obvious polarization phenomenon occurring at potentials larger than 1.7 V. Hence, 0-1.6V was selected as the operating potential window to reduce the damage to the electrode and ensure stable operation of the device.

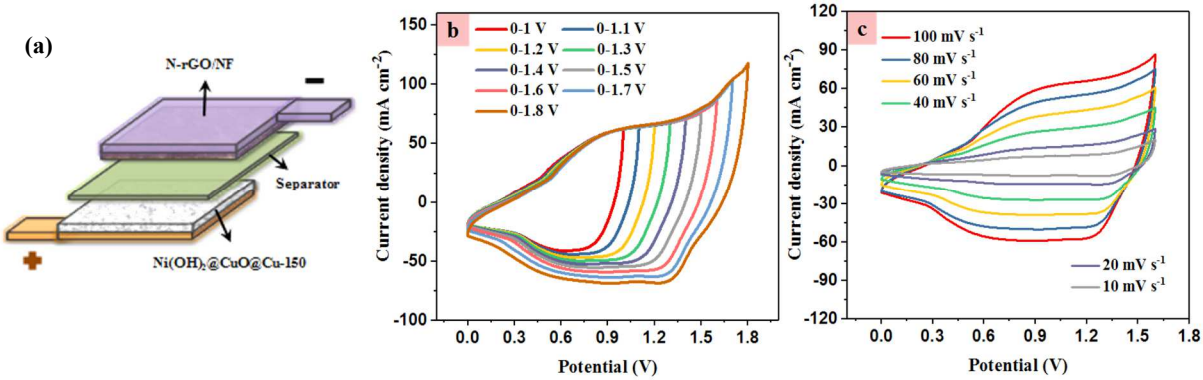

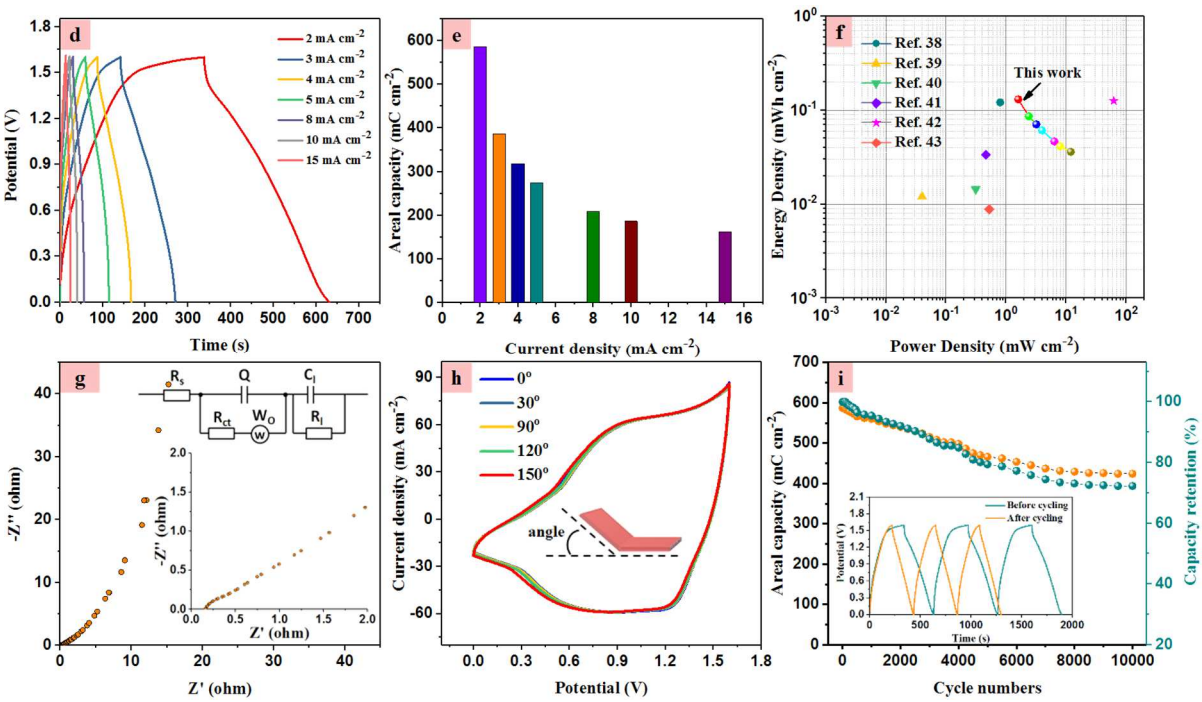

Figure 6: (a) Schematic of the packed hybrid supercapacitor device. CV plots measured at 100 mV s^{-1} for (b) different potential windows and (c) different scan rates between 0 and 1.6 V. (d) GCD curves recorded at various current densities. (e) Areal capacity obtained at various current densities. (f) Ragone plot. (g) EIS curve acquired in the frequency range of 0.01 Hz and 100 kHz; the inset up-right in (g) is the corresponding equivalent circuit. (h) CV plots acquired at 100 mV s^{-1} at different bending angles. (i) Cycling performance at 2 mA cm^{-2}; the inset in (i) are the GCD plots before and after cycling.

Figure 6c displays the CV plots acquired between 0 and 1.6 V at various scan rates, which shows a typical capacitive-like behavior of a hybrid supercapacitor device with obvious deviation from ideal capacitive characteristics [16]. Moreover, the GCD profiles at various current densities were recorded (**Figure 6d**) according to equation (S2), and the corresponding areal capacities of the hybrid supercapacitor device were calculated and displayed in **Figure 6e**. Areal capacities of 587, 387, 318, 274, 209, 186 and 162 mC cm^{-2} were obtained respectively at 2, 3, 4, 5, 8, 10 and 15 mA cm^{-2}. Accordingly, the Ragone plot related to energy density and power density, calculated by equations (S5) and (S6), is depicted in **Figure 6f**, achieving the largest areal energy density of 130.4 μWh cm^{-2} at a power density of 1.6 mW cm^{-2}. In comparison, this value is higher than that achieved by $NiCo_2S_4$//C (121

μWh cm^{-2} at 0.8 mW cm^{-2}) [38], Mn_3O_4//$Ni(OH)_2$ (12 μWh cm^{-2} at 0.04 mW cm^{-2}) [39], Ni-Co LDH//ketjenblack (14.4 μWh cm^{-2} at 312.5 μW cm^{-2}) [40], $Ni(OH)_2$-AC-based hybrid capacitor (33.6 μWh cm^{-2} at 0.46 mW cm^{-2}) [41], YP-80F//Ni_1Co_1-OH (125.6 μWh cm^{-2} at 62.16 mW cm^{-2}) [42] and RGO@CoNi-LDH//RGO@AC (8.89 μWh cm^{-2} at 0.525 mW cm^{-2}) [43] hybrid supercapacitor devices (**Table S6**).

EIS analysis was further performed in the 100 kHz to 0.01 Hz frequency range to highlight the electrochemical processes of the hybrid supercapacitor device (**Figure 6g**), showing small internal resistance (R_s=0.166 ohm cm^{-2}) and charge-transfer resistance (R_{ct}=0.438 ohm cm^{-2}).

Additionally, the mechanical characteristics and flexibility of the device were assessed by bending at various angles, as illustrated in the schematic diagram in the middle of **Figure 6h**. We can see that there was no obvious shape change of the CV plots at various bending angles (0°, 30°, 60°, 90° and 150°), signifying the good mechanical stability and enhanced flexibility of the hybrid supercapacitor device. In addition, the stability was tested for 10,000 charging-discharging cycles at 2 mA cm^{-2}. The device retained about 92% and 72% of the original capacity after 2,000 and 10,000 cycles, respectively, suggesting a good cycling stability.

To explore the potential of the device for practical applications, two as-prepared hybrid $Ni(OH)_2$@CuO@Cu-150//N-rGO/NF supercapacitor devices in series were connected to provide energy for a red LED (1.8-2 V), as illustrated in **Figure 7a**. **Figure 7b** reveals the successful lighting of the red LED powered by the devices, which can last for 12 min 39 s. Additionally, we constructed a three-digit digital display (4-30 V) with three as-prepared hybrid supercapacitor devices connected in series (**Figure 7c**). The three-digit digital display was successfully lighted up by the supercapacitor devices for 1 min 28 s (**Figure 7d**). All of these results demonstrate the promising application of the hybrid supercapacitor for flexible energy storage.

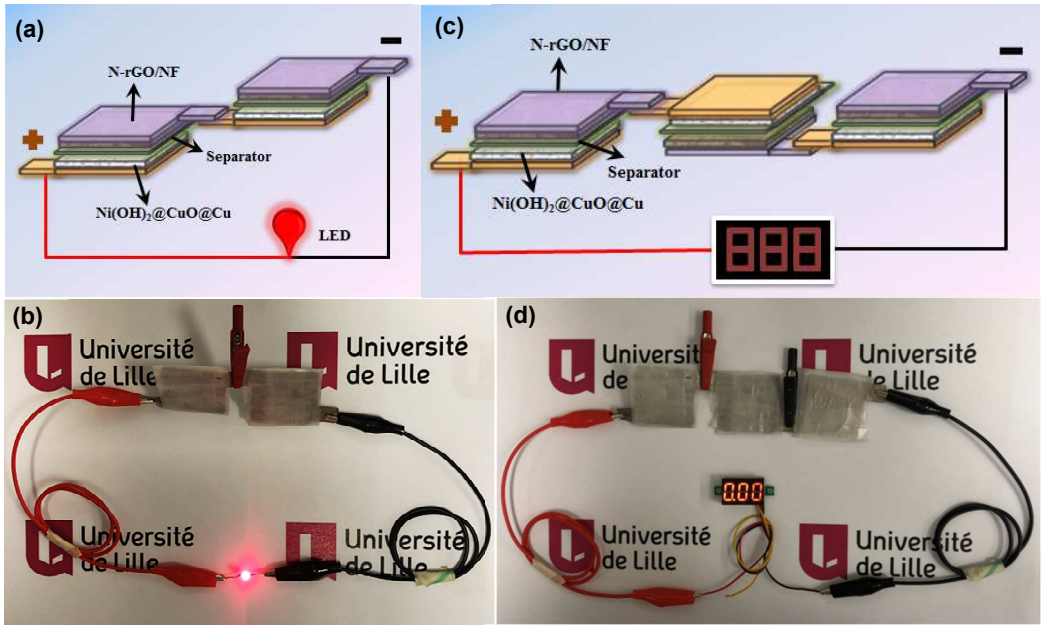

Figure 7. (a) Schematic diagram of two hybrid supercapacitor devices in series for lighting of a LED. (b) A red LED lighted up by two supercapacitor devices in series. (c) Schematic diagram of three hybrid supercapacitor devices in series for lighting a digital display. (d) A three-digit digital display lighted up by three supercapacitor devices in series.

Furthermore, taking benefit of the cleanest and earth abundant solar energy to power a hybrid supercapacitor device represents an appealing method. Therefore, solar cells were used to supply energy to the $Ni(OH)_2$@CuO@Cu-150//N-rGO/NF hybrid supercapacitor (**Figure 8a**). From the schematic diagram, we can see that the whole system comprises two steps. In the first step: the hybrid supercapacitor device was charged by solar cells, while in the second step, the hybrid supercapacitor device was used to supply electricity for a home-designed windmill device, including an engine (1.5-9 V) and a windmill. Herein, the solar cells acted as the energy conversion system, the hybrid supercapacitor device was employed as the energy storage device and home-designed windmill was applied as the energy utilization device, constituting the entire system. The entire operation process can be equivalent to the circuit diagram on the right.

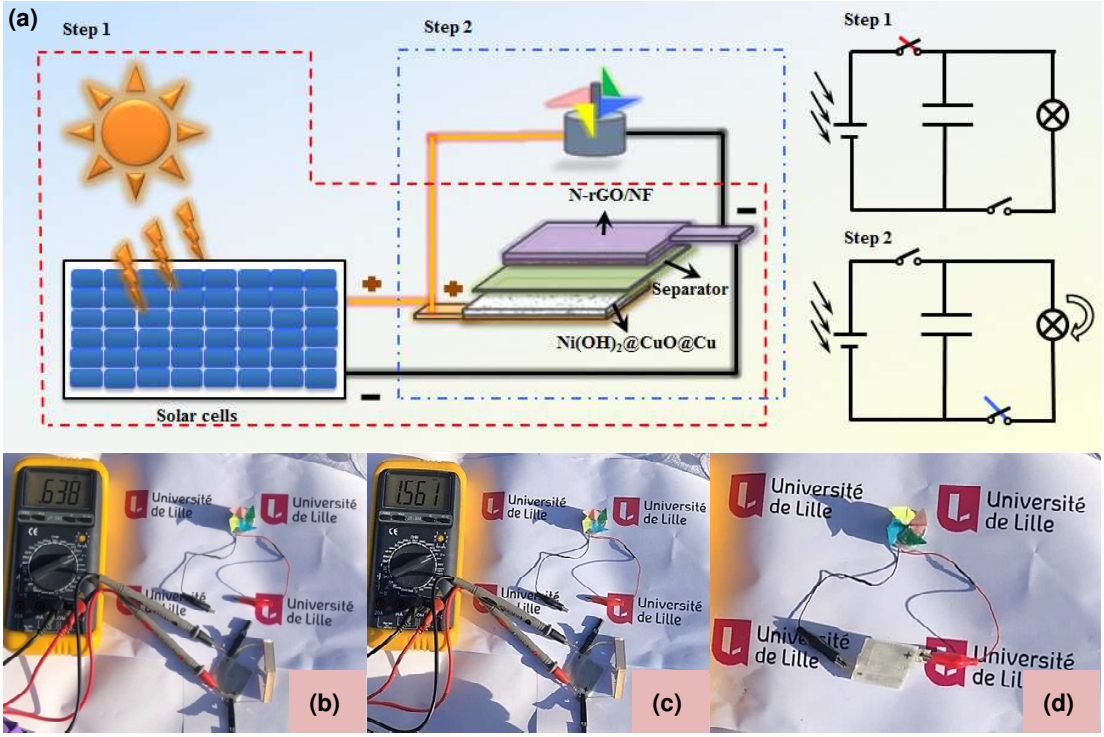

Figure 8. Schematic diagram and equivalent circuit of integrated system combining solar cells with the hybrid supercapacitor device for operating a homemade windmill device. (b-c) Photographs of the solar cells charging of the hybrid supercapacitor device. (d) Photograph of the home-designed windmill device operation.

The test was performed outdoors; the two solar cells (SC-3012-2A) connected in series were powered by sunlight from 0.638 V to 1.561 V (**Figure 8b** and **c**), and then provided energy for the home-designed windmill device (**Figure 8d**), which was continuously rotated for 59 s. At the same time, the solar cells were obtained from the abandoned solar-toy, realizing waste utilization, in line with the concept of sustainable development. All the results provided a proof for the combination of solar cells and a hybrid supercapacitor device, signifying the promising potential and direction for the energy storage devices for the future applications.

4. Conclusion

In conclusion, $Ni(OH)_2$@CuO@Cu composites were prepared by electrochemical deposition at different times (30, 50, 90, 150 and 200 s) of $Ni(OH)_2$ on CuO@Cu. Among all

the prepared electrodes, $Ni(OH)_2$@CuO@Cu-150 achieved the largest areal capacity of 7063.2 mC cm^{-2} at 20 mA cm^{-2}. Therefore, a hybrid supercapacitor consisting of $Ni(OH)_2$@CuO@Cu-150 positive and N-rGO/NF negative electrodes was assembled. The energy storage device attained a high areal energy density of 130.4 μWh cm^{-2} at a power density of 1.6 mW cm^{-2}, which are higher than many previous works [38-40]. Two hybrid supercapacitor devices in series were able to power a red LED for 12 min 39 s and three devices in series successfully supplied electricity for a three-digit digital display for 1 min 28 s. Finally, an integrated system combining solar cells with the hybrid supercapacitor device for operating a homemade windmill device was constructed. After charging by solar cells, the hybrid supercapacitor device stored energy and further powered a homemade windmill device for 59 s, achieving energy conversion, storage and utilization. All of the findings suggested that $Ni(OH)_2$@CuO@Cu composites have potential for hybrid supercapacitor devices application, and the combination of solar cells with the supercapacitor device represents a promising future for sunlight-powered energy storage device applications.

Acknowledgements

The authors gratefully acknowledge financial support from the Centre National de la Recherche Scientifique (CNRS), the University of Lille, and the Hauts-de-France region. Min Li thanks Chinese government for the China Scholarship Council fellowship.

Conflict of interest

No conflict of interest to declare.

References

[1] P. Zhao, M. Yao, H. Ren, N. Wang, S. Komarneni, Nanocomposites of hierarchical ultrathin MnO_2 nanosheets/hollow carbon nanofibers for high-performance asymmetric supercapacitors, Appl. Surf. Sci. 463 (2019) 931-938.

[2] Y. Ouyang, H. Ye, X. Xia, X. Jiao, G. Li, S. Mutahir, L. Wang, D. Mandler, W. Lei, Q. Hao, Hierarchical electrodes of $NiCo_2S_4$ nanosheets-anchored sulfur-doped Co_3O_4 nanoneedles with advanced performance for battery-supercapacitor hybrid devices, J. Mater.

Chem. A 7 (2019) 3228-3237.

[3] Z. Tian, X. Tong, G. Sheng, Y. Shao, L. Yu, V. Tung, J. Sun, R.B. Kaner, Z. Liu, Printable magnesium ion quasi-solid-state asymmetric supercapacitors for flexible solar-charging integrated units, Nat. Commun. 10 (2019) 4913.

[4] Y. Yuan, Y. Lu, B.E. Jia, H. Tang, L. Chen, Y.J. Zeng, Y. Hou, Q. Zhang, Q. He, L. Jiao, J. Leng, Z. Ye, J. Lu, Integrated System of Solar Cells with Hierarchical $NiCo_2O_4$ Battery-Supercapacitor Hybrid Devices for Self-Driving Light-Emitting Diodes, Nano-Micro Lett. 11 (2019) 42.

[5] J.H. Zhang, M.J. Wei, Z.W. Wei, M. Pan, C.Y. Su, Ultrathin Graphitic Carbon Nitride Nanosheets for Photocatalytic Hydrogen Evolution, ACS Appl. Nano Mater. 3 (2020) 1010-1018.

[6] H. Qiu, S. An, X. Sun, H. Yang, Y. Zhang, W. He, MWCNTs-GONRs/Co_3O_4@$Ni(OH)_2$ core-shell array structure with a high performance electrode for supercapacitor, Chem. Eng. J. 380 (2020) 122490.

[7] Y.L. Liu, C. Yan, G.G. Wang, H.Y. Zhang, L.Y. Dang, B.W. Wu, Z.Q. Lin, X.S. An, J.C. Han, Achieving Ultrahigh Capacity with Self-Assembled $Ni(OH)_2$ Nanosheet-Decorated Hierarchical Flower-like $MnCo_2O_{4.5}$ Nanoneedles as Advanced Electrodes of Battery-Supercapacitor Hybrid Devices, ACS Appl. Mater. Interfaces 11 (2019) 9984-9993.

[8] T.G. Yun, M. Park, D.H. Kim, D. Kim, J.Y. Cheong, J.G. Bae, S.M. Han, I.D. Kim, All-Transparent Stretchable Electrochromic Supercapacitor Wearable Patch Device, ACS Nano 13 (2019) 3141-3150.

[9] Y.F. Wang, S.X. Zhao, L. Yu, X.X. Zheng, Q.L. Wu, G.Z. Cao, Design of multiple electrode structures based on nano Ni_3S_2 and carbon nanotubes for high performance supercapacitors, J. Mater. Chem. A 7 (2019) 7406-7414.

[10] A.K. Farquhar, S.R. Smith, C.V. Dyck, R.L. McCreery, Large Capacity Enhancement of Carbon Electrodes by Solution Processing for High Density Energy Storage, ACS Appl. Mater. Interfaces 12 (2020) 1.211-10223.

[11] H. Jia, J. Sun, X. Xie, K. Yin, L. Sun, Cicada slough-derived heteroatom incorporated porous carbon for supercapacitor: Ultra-high gravimetric capacitance, Carbon 143 (2019) 309-317.

[12] J. Huang, Z. Peng, Y. Xiao, Y. Xu, L. Chen, Y. Xiong, L. Tan, K. Yuan, Y. Chen, Hierarchical Nanosheets/Walls Structured Carbon-Coated Porous Vanadium Nitride Anodes Enable Wide-Voltage-Window Aqueous Asymmetric Supercapacitors with High Energy Density, Adv. Sci. 6 (2019) 1900550.

[13] J. Huang, Y. Xiao, Z. Peng, Y. Xu, L. Li, L. Tan, K. Yuan, Y. Chen, Co_3O_4 Supraparticle-Based Bubble Nanofiber and Bubble Nanosheet with Remarkable Electrochemical Performance, Adv. Sci. 6 (2019) 1900107.

[14] S. Li, P. Cheng, J. Luo, D. Zhou, W. Xu, J. Li, R. Li, D. Yuan, High-Performance Flexible Asymmetric Supercapacitor Based on CoAl-LDH and rGO Electrodes, NanoMicro Lett. 9 (2017) 31.

[15] Y.P. Lin, N.L. Wu, Characterization of $MnFe_2O_4/LiMn_2O_4$ aqueous asymmetric supercapacitor, J. Power Sources 196 (2011) 851-854.

[16] Y. Shao, M.F. El-Kady, J. Sun, Y. Li, Q. Zhang, M. Zhu, H. Wang, B. Dunn, R.B. Kaner, Design and Mechanisms of Asymmetric Supercapacitors, Chem. Rev. 118 (2018) 9233-9280.

[17] Q. Wang, Y. Zhang, H. Jiang, T. Hu, C. Meng, In Situ Generated $Ni_3Si_2O_5(OH)_4$ on Mesoporous Heteroatom-Enriched Carbon Derived from Natural Bamboo Leaves for High-Performance Supercapacitors, ACS Appl. Energy Mater. 1 (2018) 3396-3409.

[18] Q. Wang, Y. Zhang, H. Jiang, X. Li, Y. Cheng, C. Meng, Designed mesoporous hollow sphere architecture metal (Mn, Co, Ni) silicate: A potential electrode material for flexible all solid-state asymmetric supercapacitor, Chem. Eng. J. 362 (2019) 818-829.

[19] X. Dong, Y. Zhang, Q. Wang, X. Zhang, M. Gao, M. Changgong, Synthesis of urchin-like $Ni_3Si_2O_5(OH)_4$ hierarchical hollow spheres/GO composite with enhanced electrochemical properties for high-performance hybrid supercapacitors, Dalton Trans. 48 (2019) 11749-11762.

[20] Z. Zhang, H. Huo, J. Gao, Z. Yu, F. Ran, L. Guo, S. Lou, T. Mu, X. Yin, Q. Wang, G. Yin, Ni-MOF derived NiO/C nanospheres grown in situ on reduced graphene oxide towards high performance hybrid supercapacitor, J. Alloys Compd. 801 (2019) 158-165.

[21] Q. Wang, Y. Zhang, J. Xiao, H. Jiang, X. Li, C. Meng, A novel ordered hollow spherical nickel silicate-nickel hydroxide composite with two types of morphologies for enhanced electrochemical storage performance, Mater. Chem. Front. 3 (2019) 2090-2101.

[22] H. Jiang, Y. Guo, T. Wang, P.L. Zhu, S. Yu, Y. Yu, X.Z. Fu, R. Sun, C.P. Wong, Electrochemical fabrication of $Ni(OH)_2$/Ni 3D porous composite films as integrated capacitive electrodes, RSC Adv. 5 (2015) 12931-12936.

[23] X. Xiong, D. Ding, D. Chen, G. Waller, Y. Bu, Z. Wang, M. Liu, Three-dimensional ultrathin $Ni(OH)_2$ nanosheets grown on nickel foam for high-performance supercapacitors, Nano Energy 11 (2015) 154-161.

[24] Q. Zou, D. Khalafallah, Z. Wu, J. Chen, M. Zhi, Z. Hong, Supercritical ethanol deposition of $Ni(OH)_2$ nanosheets on carbon cloth for flexible solid-state asymmetric supercapacitor electrode, J. Supercrit. Fluid. 159 (2020) 104774.

[25] D. Shi, L. Zhang, X. Yin, T.J. Huang, H. Gong, A one step processed advanced interwoven architecture of $Ni(OH)_2$ and Cu nanosheets with ultrahigh supercapacitor performance, J. Mater. Chem. A 4 (2016) 12144-12151.

[26] R. Li, Z. Hu, X. Shao, P. Cheng, S. Li, W. Yu, W. Lin, D. Yuan, Large Scale Synthesis of NiCo Layered Double Hydroxides for Superior Asymmetric Electrochemical Capacitor, Sci. Rep. 6 (2016) 18737.

[27] P. Sirisinudomkit, P. Iamprasertkun, A. Krittayavathananon, T. Pettong, P. Dittanet, M. Sawangphruk, Hybrid Energy Storage of $Ni(OH)_2$-coated N-doped Graphene Aerogel//N-doped Graphene Aerogel for the Replacement of NiCd and NiMH Batteries, Sci. Rep. 7 (2017) 1124.

[28] H.Y. Chen, H.J. Niu, X. Ma, J.J. Feng, X. Weng, H. Huang, A.J. Wang, Flower-like platinum-cobalt-ruthenium alloy nanoassemblies as robust and highly efficient electrocatalyst for hydrogen evolution reaction, J. Colloid Interface Sci. 561 (2020) 372-378.

[29] Z. Han, A.J. Wang, L. Zhang, Z.G. Wang, K.M. Fang, Z.Z. Yin, J.J. Feng, 3D highly branched PtCoRh nanoassemblies: Glycine-assisted solvothermal synthesis and superior catalytic activity for alcohol oxidation, J. Colloid Interface Sci. 554 (2019) 512-519.

[30] J. Yuan, J.J. Zhang, M.P. Yang, W.J. Meng, H. Wang, J.X. Lu, CuO Nanoparticles Supported on TiO_2 with High Efficiency for CO_2 Electrochemical Reduction to Ethanol, Catalysts 8 (2018) 171.

[31] T. Zhou, Z. Cao, P. Zhang, H. Ma, Z. Gao, H. Wang, Y. Lu, J. He, Y. Zhao, Transition metal ions regulated oxygen evolution reaction performance of Ni-based hydroxides

hierarchical nanoarrays, Sci. Rep. 7 (2017) 46154.

[32] A. Devadoss, P. Sudhagar, C. Ravidhas, R. Hishinuma, C. Terashima, K. Nakata, T. Kondo, I. Shitanda, M. Yuasa, A. Fujishima, Simultaneous glucose sensing and biohydrogen evolution from direct photoelectrocatalytic glucose oxidation on robust Cu_2O-TiO_2 electrodes, Phys. Chem. Chem. Phys. 16 (2014) 21237-21242.

[33] Y. Cheng, Y. Zhang, H. Jiang, X. Dong, C. Meng, Z. Kou, Coupled cobalt silicate nanobelt-on-nanobelt hierarchy structure with reduced graphene oxide for enhanced supercapacitive performance, J. Power Sources 448 (2020) 227407.

[34] Y. Zhang, C. Wang, H. Jiang, Q. Wang, J. Zheng, C. Meng, Cobalt-nickel silicate hydroxide on amorphous carbon derived from bamboo leaves for hybrid supercapacitors, Chem. Eng. J. 375 (2019) 121938.

[35] Q. Wang, Y. Zhang, H. Jiang, C. Meng, In-situ grown manganese silicate from biomass-derived heteroatom-doped porous carbon for supercapacitors with high performance, J. Colloid Interface Sci. 534 (2019) 142-155.

[36] Y. Zhang, H. Jiang, Q. Wang, C. Meng, In-situ hydrothermal growth of $Zn_4Si_2O_7(OH)_2{\cdot}H_2O$ anchored on 3D N, S-enriched carbon derived from plant biomass for flexible solid-state asymmetrical supercapacitors, Chem. Eng. J. 352 (2018) 519-529.

[37] Y. Cheng, Y. Zhang, C. Meng, Template Fabrication of Amorphous Co_2SiO_4 Nanobelts/Graphene Oxide Composites with Enhanced Electrochemical Performances for Hybrid Supercapacitors, ACS Appl. Energy Mater. 2 (2019) 3830-3839.

[38] W. Kong, C. Lu, W. Zhang, J. Pu, Z. Wang, Homogeneous core-shell $NiCo_2S_4$ nanostructures supported on nickel foam for supercapacitors, J. Mater. Chem. A 3 (2015) 12452-12460.

[39] J.X. Feng, S.H. Ye, X.F. Lu, Y.X. Tong, G.R. Li, Asymmetric Paper Supercapacitor Based on Amorphous Porous Mn_3O_4 Negative Electrode and $Ni(OH)_2$ Positive Electrode: A Novel and High-Performance Flexible Electrochemical Energy Storage Device, ACS Appl. Mater. Interfaces 7 (2015) 11444-11451.

[40] M. Yang, H. Cheng, Y. Gu, Z. Sun, J. Hu, L. Cao, F. Lv, M. Li, W. Wang, Z. Wang, S. Wu, H. Liu, Z. Lu, Facile electrodeposition of 3D concentration-gradient Ni-Co hydroxide nanostructures on nickel foam as high performance electrodes for asymmetric supercapacitors,

Nano Res. 8 (2015) 2744-2754.

[41] H.B. Li, M.H. Yu, F.X. Wang, P. Liu, Y. Liang, J. Xiao, C.X. Wang, Y.X. Tong, G.W. Yang, Amorphous nickel hydroxide nanospheres with ultrahigh capacitance and energy density as electrochemical pseudocapacitor materials, Nat. Commun. 4 (2013) 1894.

[42] Z. Li, S. He, C. Ji, H. Mi, C. Lei, Z. Li, H. Pang, Z. Fan, C. Yu, J. Qiu, Hierarchical Bimetallic Hydroxides Built by Porous Nanowire-Lapped Bundles with Ultrahigh Areal Capacity for Stable Hybrid Solid‐State Supercapacitors, Adv. Mater. Interfaces 6 (2019) 1900959.

[43] Q. Yin, D. Li, J. Zhang, Y. Zhao, C. Wang, J. Han, CoNi-layered double hydroxide array on graphene-based fiber as a new electrode material for microsupercapacitor, Appl. Surf. Sci. 487 (2019) 1-8.
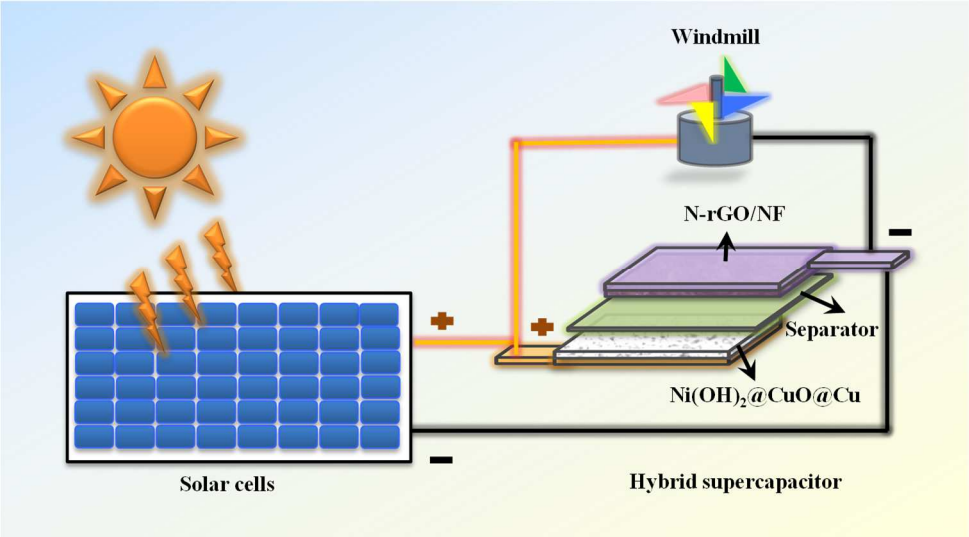
Graphical abstract